



Applying a diagnostic equation for maximum urban heat island intensity based on local climate zones for Guangzhou, China

Guang Chen^a, Hao He^a, Yiqi Chen^a, Lihua Zhao^{b,c}, Yunnan Cai^{a,*}, Yuan Ma^a

^a School of Architecture and Urban Planning, Guangdong University of Technology, Guangzhou, 510090, China

^b School of Architecture, South China University of Technology, Guangzhou, 510641, China

^c State Key Laboratory of Subtropical Building Science, South China University of Technology, Guangzhou, 510641, China



ARTICLE INFO

Keywords:

Urban heat island
Diagnostic equation
Local climate zone
Spatiotemporal variation
Guangzhou

ABSTRACT

The Urban Heat Island (UHI) is a widely studied phenomenon, characterized by unique spatiotemporal variations depending on urban structure. Seeking a simple and rapid method to monitor the Urban Heat Island Intensity (*UHII*) for local urban area with multiple inner morphology is essential for energy saving, citizen health, and urban planning. Hence, this study proposed a diagnostic equation for daily maximum urban heat island intensity ($UHII_{max}$) based on routine meteorological data and basic urban properties. The applicability of equation, previously proposed by European scholars, was evaluated based on Local Climate Zone (LCZ) scheme by a long-term temperature observation experiment conducted in Guangzhou. Overall, the underestimation of $UHII_{max}$ was caused by LCZ_{1,2,3,4}, in which the morphological parameters were outside the application range of the original equation. Then, a revised equation was proposed by adding the impervious surface fraction (ISF) in morphological parameters based on the spatiotemporal variance of *UHII* for different LCZ. The revised equation was evaluated against a year dataset and revealed a higher accuracy than the original one with a decrease of RMSE and MEAE at 0.4K, 0.15K, an increase of d_r at 0.1. Moreover, the efficiency of the equations for all the seasons and LCZs were elucidated. In summary, the results can be used as a tool for monitoring the development of UHI in outdoor temperature studies.

1. Introduction

Under the accelerated urbanization and strengthening climate change, the urban heat island (UHI) effect has become one of most dynamically changing and well-documented climate effects. UHI intensity (*UHII*) is normally defined as the difference in near-surface air temperature between urban areas and suburban areas. This occurs due to an energy imbalance [1]: urban geometry and the density of development are known to influence processes such as the trapping of both incoming solar and outgoing long-wave radiation, the reduction of turbulent transport due to wind shelter and the amount of anthropogenic heat released, which cause temperature difference between urban areas and suburban areas. The daily maximum UHI intensity ($UHII_{max}$) can be regarded as an indicator of the UHI development. In turn, the UHI markedly affects the thermal comfort [2,3], energy consumption [4,5] and ecological security factors such as phenological disorders of vegetation [6,7], especially in hot and humid cities.

A myriad of factors considerably influence the development of UHIs,

such as geographical location, topography, morphology and demography, land cover and land use, and anthropogenic heat emissions, all fundamentally affect the development of UHI [8,9]. Moreover, meteorological conditions [10–12] such as precipitation, solar radiation, wind speed and direction, cloud cover, all contribute to the intensity of UHI as well. As numerous parameters affect the development of UHI, there is a growing corpus of methods aimed at the quantification of this phenomenon. In general, the methods for studying UHI can be classified into four categories. First, field measurements of UHI based on observations represent the most traditional method for studying UHI [13]. Field measurements have been broadly utilized in studies, addressing the relationship between UHI and multiple urban elements, such as green space layouts [14,15], water bodies [16,17] and street canyon [18,19]. However, such studies focused on the urban-rural dichotomy without considering the urban local characteristics. To close this gap, Stewart and Oke [20] proposed to use the Local Climate Zone (LCZ) theory and has been widely used in thermal environment study [21,22]. Despite the promising results, the aforementioned method suffers from the

* Corresponding author.

E-mail address: caiyunnan@gdut.edu.cn (Y. Cai).

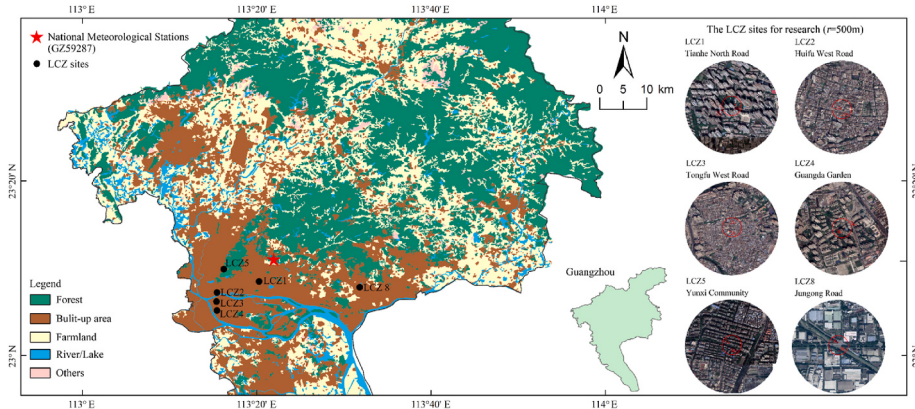


Fig. 1. The LCZ distribution in Guangzhou city.

quantitative dearth of observations, thereby limiting the understanding of spatiotemporal patterns of UHI. Second, remote sensing technology, combined with the LCZ scheme, has been applied to resolve spatiotemporal characteristics of UHI in such metropolitan areas as Yangtze River Delta cities including Shanghai, Nanjing and Hangzhou [23], Pearl River Delta cities Guangzhou and Hong Kong [24] and in some European and American cities [25,26]. Third, numerical simulations have been actively applied in recent years in UHI research, thereby revealing a variety of parameters such as air temperature, relative humidity, wind speed, solar radiation, and other thermal attributes. In this way, one can analyze the thermal environment characteristics based on a three-dimensional perspective. In this context, large number of numerical models have been developed to satisfy the objectives of various scales of research [27,28]. All the three methods are usually combined in research, but it is challenging to apply them either by once or in synergy in practice.

Finally, there is another potential approach based on an analytical formula-based calculation of *UHII*. The analytical methods are simple and easy to apply as the final equation can be obtained by linear regression or based on dimensional analysis. Urban form indicator and urban development index have been already applied for analyzing the relationship with the *UHII* in Jing-Jin-Ji region of China according to the following formula: $UHII = \beta_1 \cdot \ln UFI + \beta_2 \cdot \ln UDI + \beta_3 \cdot \ln UFI \cdot \ln UDI + u$ [29], where *UFI* is the urban form indicator, *UDI* refers to urban development index and *u* is a constant. However, this equation can only be used for calculating the annual development level of *UHII*, while the variations in smaller temporal scale should be taken into consideration as well. Moreover, a previous study combined three indicators (city size, fractal dimension, anisometry) with the *UHII* in European cities, thereby acquiring the formula based on logarithmic functions ($\Delta T = a + b \cdot \ln S_C + c \cdot D_f + d \cdot \ln A + e \cdot D_f \cdot \ln S_C + f \cdot D_f \cdot \ln A + g \cdot \ln S_C \cdot \ln A + h \cdot D_f \cdot \ln S_C \cdot \ln A$), where the *S_C* is the urban cluster size, *D_f* and *A* refers to fractal dimension and anisometry, respectively [30]. Despite their advantages, the equations based on linear regression requires long time and large amounts of fundamental observations, thereby hindering their applications for only certain cities. To this end, Theeuwes et al. [31] markedly simplified the equation based on dimensional analysis by introducing a diagnostic equation of daily maximum *UHII*, for which routine meteorological parameters and simple urban morphological properties are required. Notably, this equation can provide a first-order estimation of *UHII_{max}*, thereby representing a useful non-expert tool [31]. Their equation was validated in 14 European cities by field measurements data. In Nanjing, China [32], seven LCZs were selected to evaluate this equation, but the results were somewhat moderate as the *UHII_{max}*, was slightly overestimated. The overestimation indicates that the equation needs to be revised according to city characteristics, different from those in Europe. Moreover, an extension study was conducted for Xi'an (China), where a new equation was proposed according

to three spatial categories. The diagnostic accuracy has been significantly improved, thereby providing an efficient tool for diagnosing the *UHII_{max}* for the Xi'an city [33]. This study about Xi'an indicates that aforementioned study in Europe has provided a fundamental equation to be applied in different Chinese cities. Indeed, the methodology should be modified, being tailored to the urban spatial morphology of an analyzed city. In particular, this equation has not been estimated and revised in hot and humid areas, while taking into account the LCZ scheme. Given the urban form variance in Guangzhou, a precise and rapid estimation method of *UHII*, applicable for multiple urban characteristics should be explored.

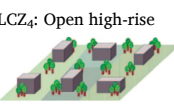
To this end, our study evaluates and revises the diagnostic equation for the daily maximum urban heat island intensity proposed by Theeuwes [31] for Guangzhou, a city with a typical subtropical climate and highly heterogeneous urban space, different from Europe. From the methodological perspective, annual hourly observation data from different Local Climate Zones (LCZs) are applied to evaluate the performance of the daily maximum *UHII* (*UHII_{max}*) diagnostic equation. On this basis, the two revised equations for different LCZs are proposed and evaluated according to the result of spatiotemporal characteristics of *UHII* (*UHII_{max}*) in six selected LCZs and diagnostic bias analysis. Overall, we expect that the proposed equation will become a useful method for studying UHI in Chinese hot and humid cities, while the results of this study will be beneficial for predicting intense UHI events as well.

2. Material and methods

2.1. Study area

Guangzhou is a city for hot and humid areas (coordinates: 112.8°E–114.2°E, 22.3°N–24.1°N), where topography is mainly hilly and the terrain is high in the northeast and low in the southwest. The average annual estimates of temperature and relative humidity in Guangzhou are 22 °C and 77%, respectively. The city is located in southern China, in the lower reaches of the Pearl River, bordering the South China Sea. The climate in Guangzhou is characterized by hot summers and warm winters and belongs to south of hot summer and warm winter area according to China's building thermal zoning, while the climate is classified as Cfa (C: warm temperate; f: fully humid; a: hot summer) by the Köppen-Geiger system [34]. The dominant wind direction in summer is southeast and in winter is north with the average wind speed of 1.5 m/s and 2.4 m/s, respectively. The *UHII* in autumn and winter with an average level of 1.5 °C is higher than that of spring and summer with an average level of 1.2 °C) [35]. Moreover, the city experiences strong *UHII* and weak *UHII* in nighttime and daytime, respectively [36]. The urban areas of Guangzhou have been rapidly expanding in 1987–2015, corresponding to the annual growth rate of 38.72 km² per year [37]. As a result, Guangzhou has become a megacity

Table 1
Morphology indicators of each LCZs.

Building type	Satellite Images		Zone parameters	Indicator range for the LCZ	
LCZ ₁ : Compact high-rise				H/W:2.24 SVF:0.48 BSF:30.55% ISF:49.28% HRE:35 m surface albedo:0.15 TRC:8 (commercial; residential) H/W:1.06 SVF:0.53 BSF:42.70% ISF:54.69% HRE:19 m surface albedo:0.11 TRC:6	H/W: > 2 SVF:0.2–0.4 BSF:40%–60% ISF:40%–60% HRE: > 25 m surface albedo:0.10–0.20 TRC:8 H/W:0.75–2 SVF:0.3–0.6 BSF:40%–70% ISF:30%–50% HRE:10–25 m surface albedo:0.10–0.20 TRC:6–7
LCZ ₂ : Compact midrise				H/W:0.84 SVF:0.57 BSF:44.86% ISF:51.61% HRE:11 m surface albedo:0.12 TRC:6 (residential; commercial) H/W:0.84 SVF:0.57 BSF:44.86% ISF:51.61% HRE:11 m surface albedo:0.12 TRC:6	H/W:0.75–1.5 SVF:0.2–0.6 BSF:40%–70% ISF:20%–50% HRE:3–10 m surface albedo:0.10–0.20 TRC:6
LCZ ₃ : Compact low-rise				H/W:1.13 SVF:0.56 BSF:26.14% ISF:56.93% HRE:28 m surface albedo:0.14 TRC:6 (residential) H/W:1.13 SVF:0.56 BSF:26.14% ISF:56.93% HRE:28 m surface albedo:0.14 TRC:6	H/W:0.75–1.25 SVF:0.5–0.7 BSF:20%–40% ISF:30%–40% HRE:>25 m surface albedo:0.12–0.25 TRC:6
LCZ ₄ : Open high-rise				H/W:0.83 SVF:0.51 BSF:28.21% ISF:55.27% HRE:20 m TRC:6 (residential) H/W:0.83 SVF:0.51 BSF:28.21% ISF:55.27% HRE:20 m TRC:6 surface albedo:0.12	H/W:0.3–0.75 SVF:0.5–0.8 BSF:20%–40% ISF: 30%–50% HRE:10m–25 m surface albedo:0.12–0.25 TRC:5–6
LCZ ₅ : Open mid-rise				H/W:0.18 SVF:0.73 BSF:36.31% ISF:35.60%* HRE:5 m surface albedo:0.21 TRC:5 (residential; campus) H/W:0.18 SVF:0.73 BSF:36.31% ISF:35.60%* HRE:5 m surface albedo:0.21 TRC:5	H/W:0.1–0.3 SVF:> 0.7 BSF:30–50% ISF:40%–50% HRE:3–10 m surface albedo:0.15–0.25 TRC:5
LCZ ₈ : Large low-rise				(commercial)	

H/W: aspect ratio; SVF: sky view factor; BSF: building surface fraction; ISF: impervious surface fraction; HRE: height of roughness elements; TRC: terrain roughness class, *represents the value deviates from parameter range of the corresponding LCZ types.

with the population of >18.6 million [38], which can potentially increase the emission of the anthropogenic heat [39]. As shown in Fig. 1, more rural farmlands, represented by large yellow areas, are located adjacent to the estuary in Guangzhou. The large green areas are mainly represented by evergreen trees or shrubs where the terrain is low elevation mountains. The urban morphology is diverse and heterogeneous, where most city buildings are air-conditioned in the summer.

2.2. A diagnostic equation for the daily $UHII_{max}$

The diagnostic equation proposed by Theeuwes et al. [31] was adopted:

$$UHII_{max} = (2 - SVF - F_{veg}) \sqrt{\frac{S_{\downarrow} DTR^3}{U}} \quad (1)$$

Where:

SVF is the sky-view factor.

F_{veg} is the surface vegetation fraction at the LCZs.

S_{\downarrow} is daily mean downward solar radiation in kinematic units

(Kms^{-1}). The amount of incoming radiation in W/m^2 divided by the air density and specific heat capacity (ρCp).

DTR is the diurnal difference between the maximum and minimum air temperature in suburban area (K)

U is the daily mean wind speed in rural areas at 10 m height (m/s).

The equation consists of urban morphological parameters (A_i) and meteorological parameters (F_b).

$$A_i = (2 - SVF - F_{veg}) \quad (1a)$$

$$F_b = \sqrt[4]{\frac{S_{\downarrow} DTR^3}{U}} \quad (1b)$$

Where A_i is a comprehensive indicator, reflecting the morphology characteristics of each LCZ. This equation was applied to a calibration range for $0 < F_{veg} < 0.4$, $0.2 < SVF < 0.9$ only [31]. The functional form was obtained using regression analysis based on the observations from the cities in northwestern Europe. Furthermore, F_b reflects the intensity of UHI, resulting from the background meteorological conditions [10]; Note that the functional form for the above three meteorological

parameters were developed using dimensional analysis.

2.3. LCZ site selection

The hourly air temperature measurements at six sites in Guangzhou were conducted starting from July 2019 (ongoing). These data were used to reflect temperatures of urban areas with different urban forms in Guangzhou. The sites selected for field measurement were based on the LCZ schemes to provide a standardized classification protocol for urban air temperature studies. According to the guidelines for using the LCZ classification system, suggested by Oke [20], an LCZ is defined as an area with a minimum radius of 200–500 m that has uniform features in terms of surface cover, structure, material, and human activity. Urban morphology and surface landscape were classified into 17 categories by the LCZ framework, including 10 built types and 7 land cover types. According to the methodological guidance in literature [20,40], aerial photos from unmanned aerial vehicles and remote sensing information were used, where several nearly the same morphology and land use type in the areas with a radius of 500 m were screened. Combined with field investigation, building types, underlying surface coverage, material and construction information, and vegetation coverage were all refined.

In this process, each LCZ was determined by 10 indicators related to surroundings' thermal environment involving Sky View Factor (SVF), Aspect ratio (H/W), Height of Roughness Elements (HRE), terrain roughness class, Building Surface Fraction (BSF), Impervious Surface Fraction (ISF) or Pervious Surface Fraction (PSF), Surface admittance, Surface albedo, and Anthropogenic heat output. Specifically, the HRE was extrapolated by building shadow length in the Google Earth image. The results were compared to the data acquired through Python. Note that field investigations were implemented when the deviation was large. In this context, the street aspect ratio, BSF, ISF, or PSF were fetched by field survey combined with remote sensing image data. Here, the SVF was calculated by three-dimensional microclimate software ENVI-met [41]. The vegetation coverage proportion was quantified via field sampling survey and map observations. Additionally, terrain roughness class was determined based on literature [42]. Surface albedo were acquired from Landsat 8 satellite images [43,44]. Due to the lack of related instruments and test methods, surface admittance, and anthropogenic heat flux (AHF) were not provided.

By following these methods, we selected seven LCZs of built types distributed across the city (LCZ_{1,2,3,4,5,8,10}). In this process, LCZ_{6,7,9} were not involved in this study due to a non-existence in Guangzhou. LCZ₁₀, Guangzhou Petrochemical, characterized by heavy industry area, was excluded due to the large amount of anthropogenic heat output [31]. The distribution of each LCZ is illustrated in Fig. 1, while the detailed information is summarized in Table 1.

2.4. Data

2.4.1. Field measurement air temperature in LCZs

Long-term hourly air temperature measured in six LCZs can reflect the temperature of urban areas. There were two fixed points in the core area of the LCZ sites within a radius of 100 m, as described in Fig. 1. The temp/RH data loggers (HOBO U23X-001, manufactured by Onset; U.S.) with the measurement range of 0–50 °C and an uncertainty of ±0.2 °C were placed into radiation shields and fastened at poles or streetlights. The logger was placed at a distance of >3 m from the walls and outside the tree shade to avoid the influence of any artificial heat sources, while ensuring adequate ventilation as well. The average value of the temperature readings obtained at the two measuring points was taken as the air temperature value of the LCZ site. The field instruments of each LCZ are summarized in Table 1.

2.4.2. Suburban meteorological dataset

To calculate the F_b , the meteorological parameters of the diagnostic equation, including air temperature, solar radiation, and wind speed in

Guangzhou suburban were applied. To this end, the data from the National Meteorological Station (NMS) No. 59287, a standard meteorological station, were used in this study (see a red pentagram in Fig. 1). As seen, the station is located in the northeast of the city. The suburban solar radiation, air temperature, relative humidity, precipitation, wind speed and direction, and atmospheric pressure from this station were acquired from the China Meteorological Data Service Center (CMDC, <http://data.cma.cn>).

2.4.3. Calculation of UHII

Fundamentally, UHII is defined as the difference of air temperature between the urban LCZ sites and the suburban areas, which can be described as $UHII = T_{LCZ} - T_{suburban}$. The hourly maximum observed UHII represents the development level of the UHI and can be described as $UHII_{max} = \max(T_{LCZ} - T_{suburban})$. In this way, we obtained a complete nocturnal cooling and a daytime warming process, defined as a day of 24-h span from 8:00 a.m. to 7:00 a.m. of the following day.

2.4.4. Identification of "ideal" days

In general, numerous meteorological factors affect the development of UHI, such as wind speed, wind direction, precipitation, and cloud cover [10]. The "ideal days" refer to a day that conducive to the development of UHI, and in which there are calm and clear conditions or weak winds and cloudless skies. For investigating the UHI effect better, "ideal days" should be screened. In this study, meteorological parameters were comprehensively used to determine the "ideal days". According to method of Europe [31], during a day, the hourly wind speed changes of >2 m/s, rainy events (daily total ≥0.1 mm and the following days), and fog events (average relative humidity >80%) were excluded, while the days that lacked the data (either urban LCZ sites or suburban area) were excluded. As a result, 239 days from July 2019 to April 2022 were used in the final analysis.

All the datasets were divided into two parts: (1) 147 days from July 2019 to April 2021, which correspond to dataset A. They were used to evaluate the original equation and to analyze the influence of A_i and F_b on $UHII_{max}$, respectively. Second, (2) dataset B contained the remaining 92 days from May 2021 to April 2022, which were applied in the validation of revised equation. Additionally, all the datasets were used to analyze spatiotemporal characteristics of UHII and for the seasonal performance evaluation of the revised equation.

2.5. Estimation indicators

A series of statistical evaluation indicators including Root Mean Square Error (RMSE), Median Absolute Error (MEAE) and refined Willmott's index of agreement (d_r) were selected to quantify the accuracy of the original and revised diagnostic equation model. The d_r is an enhanced indicator modified based on the Willmott's index of agreement (d). As it is regarded as more rational for describing the heterogeneity between the model and the observation [45], d_r was applied in the quantitative estimation of the diagnostic equation. The indicators were quantified based on the following equations:

$$RMSE = \sqrt{\frac{1}{m} \sum_{i=1}^m (y_i - f(x_i))^2} \quad (2)$$

$$MEAE = median(y_i - f(x_i)) \quad (3)$$

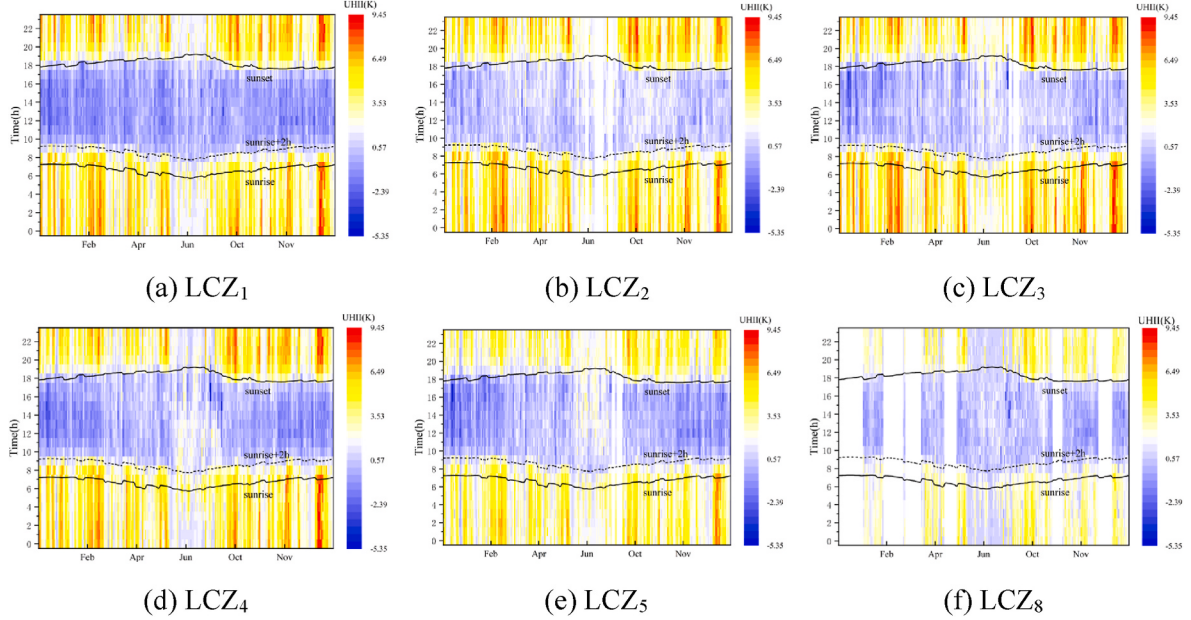


Fig. 2. Hourly *UHII* in months for LCZs during the 239 days, the white zone represents the day of missing data.

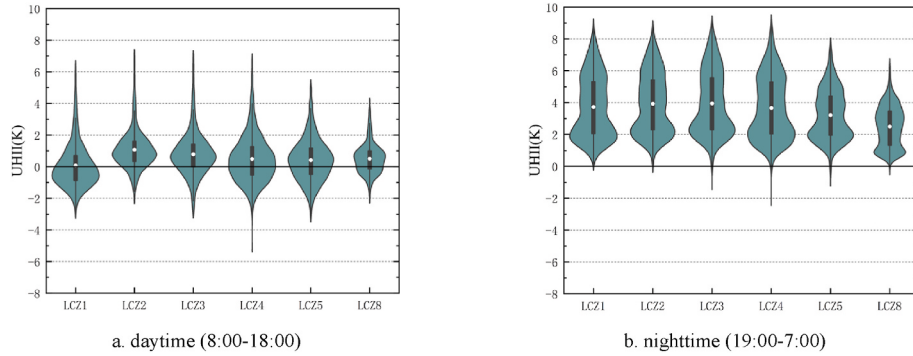


Fig. 3. Hourly *UHII* value during the daytime and nighttime for 239 days:(a) daytime; (b) nighttime, the white dots represent the average *UHII*, the black line presents the *UHII* is zero.

$$d_r = \begin{cases} 1 - \frac{\sum_{i=1}^n |y_i - f(x_i)|}{2 \sum_{i=1}^n |y_i - \bar{y}|}, & \text{if } \sum_{i=1}^n |y_i - f(x_i)| \leq 2 \sum_{i=1}^n |y_i - \bar{y}| \\ \frac{2 \sum_{i=1}^n |y_i - \bar{y}|}{\sum_{i=1}^n |y_i - f(x_i)|} - 1, & \text{if } \sum_{i=1}^n |y_i - f(x_i)| > 2 \sum_{i=1}^n |y_i - \bar{y}| \end{cases}, \quad -1 \leq d_r \leq 1 \quad (4)$$

where y_i is the observed values and $f(x_i)$ corresponds to the modelled values. Lastly, \bar{y} refers to the mean observed values.

3. Results

3.1. Characteristics of *UHII*

The hourly *UHII* characteristics at all LCZs during the 239 days are shown in Fig. 2 in the form of heatmaps. As seen, the diurnal circulation of *UHII* exhibited clear regular patterns during the whole period. Specifically, higher *UHII* was identified in the period from the sunset to 2 h after the sunrise. In contrast, lower *UHII* was registered during the time

period between 2 h after sunrise and the sunset. Moreover, a so-called Urban Cool Island (UCI), namely, the phenomenon when $T_{urban} < T_{suburban}$, was observed from sunset to sunrise during a whole year across all the LCZs. The frequency and intensity of UCI exhibited some variability. Moreover, in all the LCZs, the *UHII* in autumn and winter with a mean value of 2.44K and 2.28K were found to be higher than that in spring (1.64K) and summer (1.28K), thereby resonating with previous studies [21,35]. Compared to LCZ₅ and LCZ₈, strong *UHII* frequently occurred in LCZ_{1,2,3,4} (see abundant red and orange stripes in Fig. 2, which represent higher *UHII*).

Fig. 3 shows the diurnal *UHII* distribution in all the LCZs. Day and night were divided in accordance with sunrise+2 h and sunset time in Guangzhou. The daytime was defined as the time range from 8:00 to 18:00, while nighttime as from 19:00 to 7:00 of CST. The results demonstrated that in all the LCZs, the nighttime *UHII* was more evenly distributed, compared to daytime *UHII*. Moreover, nighttime *UHII* ranged from -2.47 to 9.41K, thereby manifesting higher values, compared to daytime (-3.16–3.99 K). The differences of mean *UHII* at each LCZ between nighttime and daytime were 3.65 K, 2.85 K, 3.16 K, 3.18 K, 2.80 K and 2.00 K in LCZ_{1~8}. Daytime *UHII* across the LCZs ranged from -5.31 to 7.36 K with the mean value of 0.56 K, whereas the nighttime *UHII* ranged between -2.47 and 9.41 K with the average of 3.55 K. The maximum *UHII* in LCZ₅ (5.95K for daytime and 7.87K for

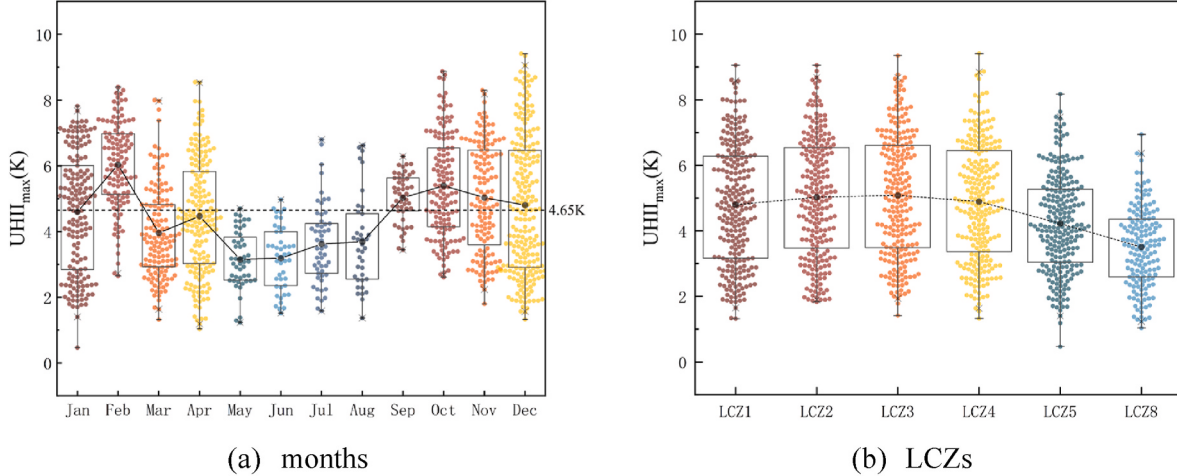


Fig. 4. Daily $UHII_{max}$ distribution (a) months (b) LCZs, the black dots represent the average values, the horizontal dashed line represents the average $UHII_{max}$ during 239 days.

nighttime) and LCZ₈ (4.70K and 6.37K) were clearly lower than that of LCZ_{1,4}(6.87K, 7.08K, 7.16K, 7.16K, respectively for daytime and 9.06K, 8.88K, 9.35K, 9.41K, respectively for nighttime). Fig. 3 demonstrates that the $UHII$ in LCZs was mostly clustered around 2 K in nighttime except LCZ₈ with ~1K, while a range of 0–1K in daytime other than LCZ₁(approximately -0.5 K). The UCI occurred frequently in daytime, especially in LCZ₁ and LCZ₄ (56.4% for LCZ₁ compared to 40.2% for LCZ₄), but almost no UCI was identified in nighttime.

Fig. 4 shows the estimates of $UHII_{max}$, reflecting the development level of $UHII$ during an entire day, where panel “a” displays the monthly daily $UHII_{max}$ distribution during the 239 days in particular. More points were discerned in autumn and winter with large number of “ideal days”, compared to spring and summer. The average $UHII_{max}$ for spring months (March, April, and May) was 4.10 K, while for summer months (June, July, and August), the mean value was 3.50 K, thereby exhibiting considerably lower estimates than the mean $UHII_{max}$ for 239 days which is 4.65 K. In contrast, the mean $UHII_{max}$ of autumnal months (September, October, and November) was 5.18 K and for winter months (December, January, February) it was 5.02 K, thereby manifesting the level exceeding 4.65 K. The maximum monthly average $UHII_{max}$ occurred in February (6.03 K) while the minimum of 3.15 K occurred in May. Fig. 4b illustrates the daily $UHII_{max}$ distribution in LCZs. Notably, it exhibited a coherent distribution trend of the similar box range for LCZ_{1,2,3,4} (3.11K, 3.06K, 3.11K, 3.08K) and LCZ_{5,8}(2.23K, 1.77K). The average $UHII_{max}$ of LCZ_{1,2,3,4} were remarkably higher than that of LCZ_{5,8}, namely, 4.80 K, 5.03 K, 5.08 K and 4.89 K for LCZ_{1,2,3,4}, 4.22 K and 3.55 K for LCZ_{5,8}, respectively.

The characteristics of $UHII$ in various seasons at the same LCZ indicate that the development of $UHII$ was governed by meteorological features. Furthermore, $UHII$ in different LCZ during the same seasons suggested that morphology played a vital role in controlling the UHI effect.

3.2. Original equation test level

3.2.1. Accuracy of model

Fig. 5 displays the prediction performance of the original equation model. Indicatively, the black dots were mostly distributed under the solid line of “y = x”, thus indicating that this equation underestimated the daily $UHII_{max}$ for LCZs. As the observed $UHII_{max}$ increased, the accuracy of the model decreased, and each LCZ experienced complete underestimations when the observed $UHII_{max}$ exceeded a certain value, represented by red dashed lines. Note that the threshold for the entire study area is 5.71 K (Fig. 5a) and is higher than the separate LCZs with a threshold range of 5–6 K except LCZ₈ (approximately 4K).

The quantitative evaluation demonstrated that the accuracy of the original equation ($RMSE = 1.47$ K, $MEAE = 0.92$ K, $d_r = 0.61$) was lower than that of northwestern Europe and Nanjing (China) but slightly higher than that of Xi'an. Moreover, different LCZ exhibited some variability in the diagnostic accuracy, as shown in Fig-s 5b–g. In this context, LCZ₅ exhibited the best performance with relatively high accuracy ($RMSE = 1.08$ K, $MEAE = 0.70$ K, $d_r = 0.64$), while the worst accuracy was demonstrated by LCZ₄ ($RMSE = 1.73$ K, $MEAE = 1.19$ K, $d_r = 0.55$). For LCZ_{1,2,3,4}, the deviation between observed $UHII_{max}$ and modelled $UHII_{max}$ was large, compared to the LCZ₅ and LCZ₈. The details of this analysis are summarized in Table 2.

3.2.2. Analysis of bias

The deviations between modelled $UHII_{max}$ and observed $UHII_{max}$ are summarized in Table 2. Here, refer to research in Xi'an [33], bias > 1.5 K is defined as overestimation, while bias < -1.5 K is defined as underestimation. It was found that LCZ_{1,2,3,4} were mostly underestimated with the following proportions of the underestimation: 27.2%, 34.8%, 38.8%, and 38.8%. Moreover, LCZ₅ and LCZ₈ exhibited similar and low proportions of underestimations of 17.1% and 16.4%, while experiencing slighter $UHII$ and $UHII_{max}$ of the six LCZs, there were no overestimation cases reported. Hence, given the temporal-spatial characteristics of $UHII$ ($UHII_{max}$), reported in section 3.1, the space can be classified into two categories: (1) LCZ_{1,2,3,4}, (2) LCZ_{5,8}

The afore-mentioned analysis indicated that the meteorological parameters acquired from dimensional analysis and urban morphology based on liner regression consisting of the equation should be separately discussed.

3.3. Influence of meteorological parameters on $UHII_{max}$

3.3.1. Single parameters (DTR , U , S^1)

Fig. 6 demonstrates the correlations between meteorological parameters (DTR , U , S^1) and $UHII_{max}$, where the Pearson's correlation coefficient (r) was used. In general, the absolute value of r reflects the linear association between variables [46]: 0–0.19 reveals “very weak”; 0.20–0.39 reveals “weak”; 0.40–0.59 reveals “moderate”; 0.60–0.79 reveals “strong”; 0.80–1.0 reveals “very strong” correlations. Note that p value of <0.05 is considered to be statistically significant.

The DTR in the suburban area is generally exposed to multiple meteorological variables on the energy balance of the rural environment [10]. The analysis of 147 days revealed a relatively stronger positive correlation between the $UHII_{max}$ and DTR ($r = 0.77$). In general, wind speed can somehow mitigate UHI, namely, enough strong wind speed can dwindle UHI down to zero. Moreover, the wind direction is also

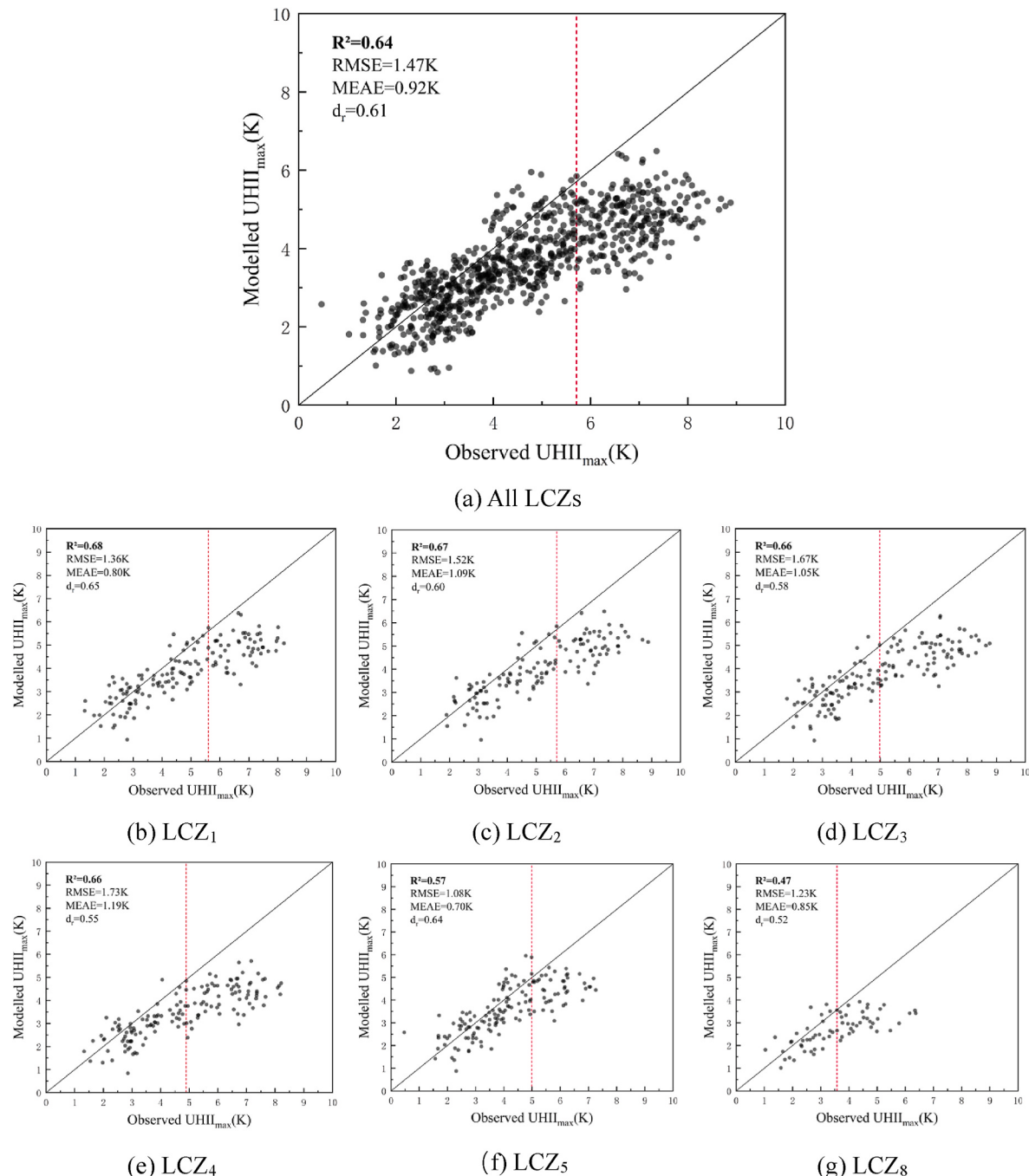


Fig. 5. The observed $UHII_{max}$ against modelled $UHII_{max}$ in equation (1)(July 2019 to April 2021), the black solid line is “ $y = x$ ”, the red dashed line represents the threshold of observed $UHII_{max}$ for underestimation. (For interpretation of the references to colour in this figure legend, the reader is referred to the Web version of this article.)

Table 2
Accuracy of original equation in all LCZs.

Indicators	All LCZs	LCZ ₁	LCZ ₂	LCZ ₃	LCZ ₄	LCZ ₅	LCZ ₈
R ²	0.64	0.68	0.67	0.66	0.66	0.57	0.47
RMSE	1.47	1.36 K	1.52 K	1.67 K	1.73 K	1.08 K	1.23 K
MEAE	0.92	0.80 K	1.09 K	1.05 K	1.19 K	0.70 K	0.85 K
d _r	0.61	0.65	0.60	0.58	0.55	0.64	0.52

essential for weakening UHII. In this context, the analysis of 147 days demonstrated a weak negative correlation ($r = -0.39$) between the $UHII_{max}$ and U. Such a weak correlation was likely due to wind speed, which did not blow in a direction that can produce a cooling effect. The weak correlation between solar radiation and UHII could be also driven by the seasonal variation for incoming solar radiation [10]. Furthermore, urban morphology such as SVF and H/W could affect the amount of solar radiation reaching ground of street canyon [47,48].

3.3.2. F_b

Fig. 7 displays the linear fit results between $UHII_{max}$ and F_b . The slope of the solid and dashed lines in the figure represents the A_i value, which

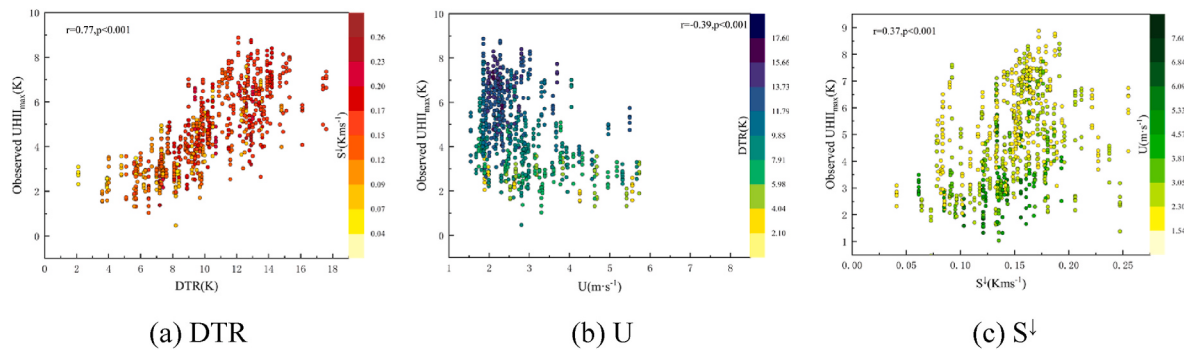


Fig. 6. Correlation between $UHII_{max}$ and meteorological parameters.

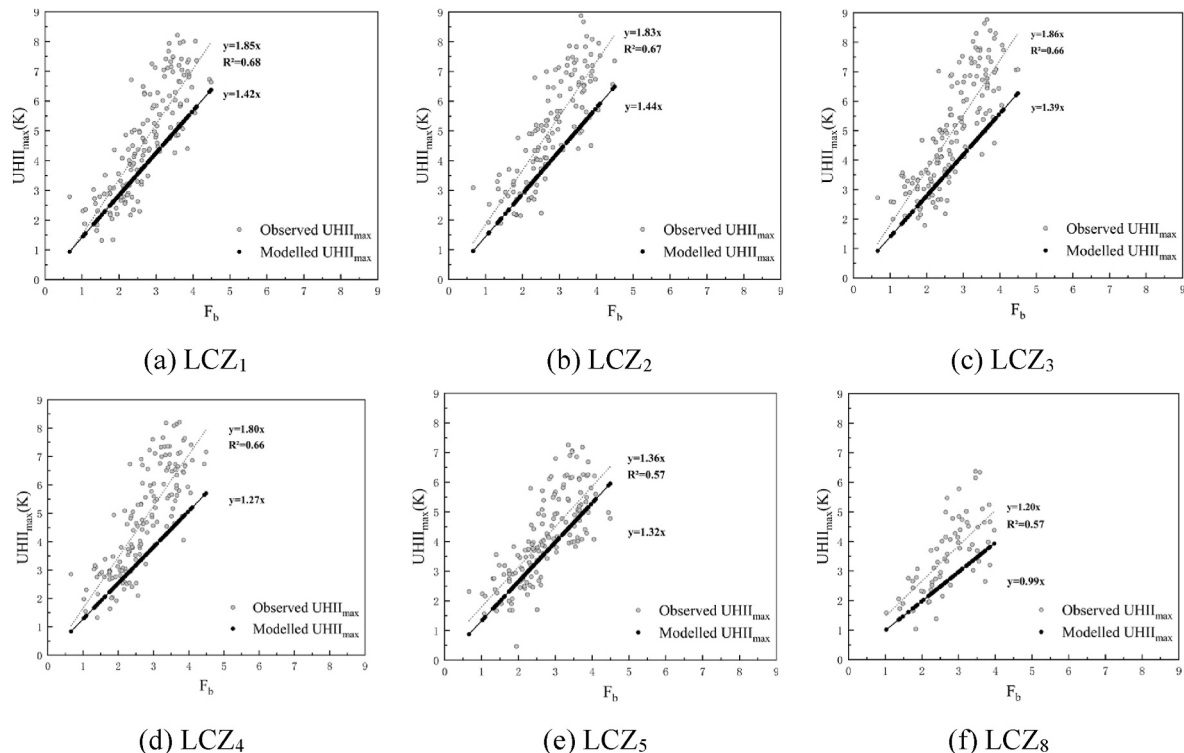


Fig. 7. Correlation between $UHII_{max}$ and F_b

Table 3
The deviations distribution of LCZs.

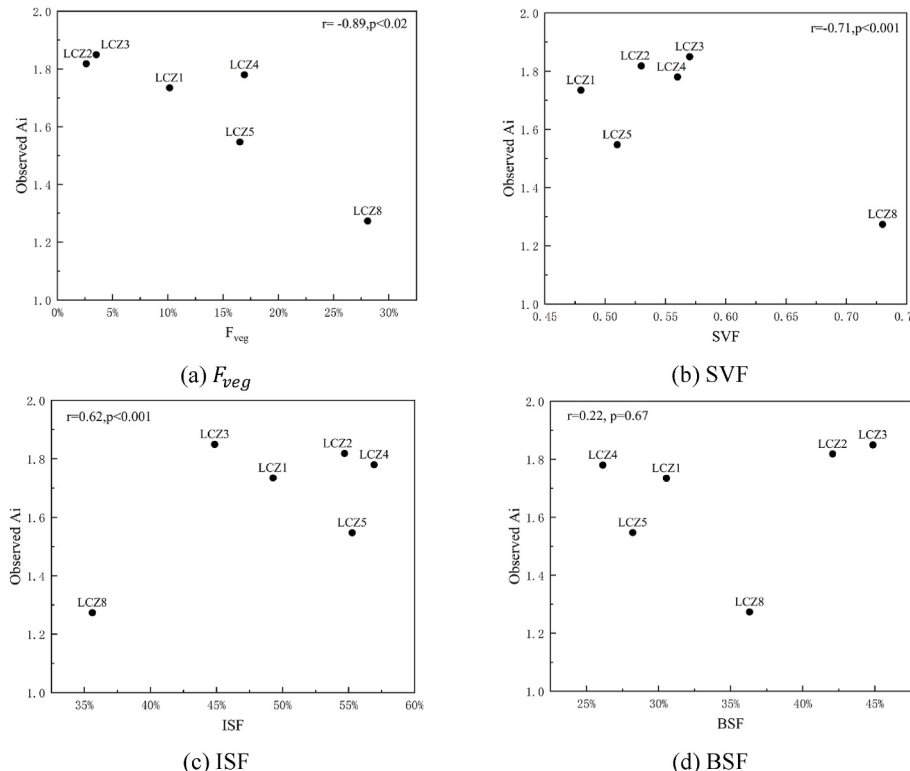
Bias interval(K)	LCZ ₁	LCZ ₂	LCZ ₃	LCZ ₄	LCZ ₅	LCZ ₈
[1.5–2]	0	0	0	0	2	0
[1–1.5]	5	2	1	1	2	1
[0.5–1]	8	3	7	5	18	3
[0–0.5)	21	19	14	10	21	7
(-0.5–0)	26	18	18	20	35	16
(-1 – -0.5]	27	22	32	30	28	15
(-1.5 – -1]	20	22	18	24	16	14
(-2 – -1.5]	16	16	21	19	14	5
(-2.5 – -2]	12	16	12	14	8	1
(-3 – -2.5]	8	9	13	10	3	5
(-3.5 – -3]	4	4	7	6	0	0
(-4 – -3.5]	0	1	4	8	0	0
Total amount	147	132	147	147	147	67
Underrated proportion	27.2%	34.8%	38.8%	38.8%	17.1%	16.4%
Overrated proportion	0	0	0	0	1.4%	0

should be theoretically closed. However, the observed slope of A_i for LCZ_{1,2,3,4} was relatively higher than modelled one, while LCZ₅ and LCZ₈ were nearly closed in contrast, the differences were listed in [Table 3](#). Note that the A_i values obtained from various methods are summarized in [Table 3](#). Moreover, the absolute value of A_i difference in LCZ₈ was slightly larger than that in LCZ₅ (0.21, 0.04). This difference was potentially driven by the missing air temperature data from October 2020 to April 2021 in LCZ₈ due to the instrumental problems. However, the identified UHII characteristics during the same period from 2019 to 2020 and from 2021 to 2022 ([Fig. 5f](#)) indicate that the observed A_i should be lower than the value of 1.20; a similar trend characteristic of LCZ₅. The F_b acquired from dimensional analysis comprehensively considers meteorological parameters according to the coefficient of determination (R^2) in all the LCZs (0.68, 0.67, 0.66, 0.66, 0.57, and 0.57). It was found that the meteorological part of equation [\(1\)](#) performed considerably well in Guangzhou. Hence, A_i can be deemed as the driver of the bias, reported in section [3.2.2](#). Note that this phenomenon might require further analysis.

Table 4

Ai value calculated via different methods.

LCZ site	Type	Observed A_i	Equation (1) A_i	Potential gap(equation (1))	Equation (5) A_i	Potential gap(equation (5))
LCZ ₁	Compact high-rise	1.85	1.42	-0.43	1.91	0.06
LCZ ₂	Compact midrise	1.83	1.44	-0.39	1.99	0.16
LCZ ₃	Compact low-rise	1.86	1.39	-0.47	1.84	-0.02
LCZ ₄	Open high-rise	1.80	1.27	-0.53	1.84	-0.04
LCZ ₅	Open mid-rise	1.36	1.32	-0.04	1.32	-0.04
LCZ ₈	Large low-rise	1.20	0.99	-0.21	0.99	-0.21

Fig. 8. The correlation between A_i and morphological parameters of LCZs: (a) F_{veg} ; (b) SVF; (c) ISF; (d) BSF.

3.4. Influence of morphology characteristics on $UHII_{max}$

In general, A_i is the synthesis of morphological characteristics. The modelled A_i corresponds to equation (1); A_i and the ideal A_i correspond to observed A_i . We defined the difference of observed A_i and modelled A_i as “potential gap” according to Fig. 7. Furthermore, the differences were calculated and details are summarized in Table 4. The application condition of the original equation was described in Section 2.2. To remind, it can be calculated as the sum of F_{veg} and SVF, which should meet the range of $0.2 < (F_{veg} + SVF) < 1.3$, which indicates the A_i is $0.7 < A_i < 1.8$. As seen from Table 3, only LCZ₅ and LCZ₈ met this requirement, while LCZ_{1,2,3,4} were found outside this range, thereby manifesting a “potential gap” of -0.43 , -0.39 , -0.47 , and -0.53 , respectively. Hence, the expansion is required to bridge the “potential gap” for approaching the ideal A_i for LCZ_{1,2,3,4}, where the “potential gap” is large.

Fig. 8 illustrates the correlation between the observed A_i and the morphological parameters of LCZs. Further, the observed A_i was calculated as the mean values for the 239 days at each LCZ. The Pearson’s correlation coefficients of SVF and F_{veg} were found to be -0.71 and -0.89 , respectively. The two parameters with strong correlation with observed A_i were also included in the initial definition of A_i from equation (1b) and were retained. Moreover, the r estimation of ISF and BSF were 0.62 and 0.22 , respectively. In previous study, ISF had been

considered as a vital indicator related to the UHII development [49–51] and was recommended in Theeuwes’ research [31]. In this study, ISF was selected as the “potential gap” to expand the A_i for LCZ_{1,2,3,4}, where the $UHII_{max}$ were markedly underestimated by the original diagnostic equation.

3.5. Expand and verify equation

According to the analysis shown above, the expanded equation (5) was proposed below. The dataset B was used to analyze the performance of this equation.

$$UHII_{max} = \begin{cases} (2 - SVF - F_{veg} + ISF) \sqrt[4]{\frac{S_1 DTR^3}{U}}, & \text{for } LCZ_{1,2,3,4} \quad (5a) \\ (2 - SVF - F_{veg}) \sqrt[4]{\frac{S_1 DTR^3}{U}}, & \text{for } LCZ_{5,8} \quad (5b) \end{cases}$$

Fig. 9a shows the comparison between the modelled $UHII_{max}$ and the observed $UHII_{max}$ using equation (5). As seen, the red dots were clearly more evenly distributed on both sides of the “y = x” line than black dots, particularly when the observed $UHII_{max}$ exceeded the complete underestimation threshold of approximately 5 K. However, it exhibited an over-correction trend for the revised model (equation (5a)) when the observed $UHII_{max}$ was lower. Notably, the accuracy of equation (5)

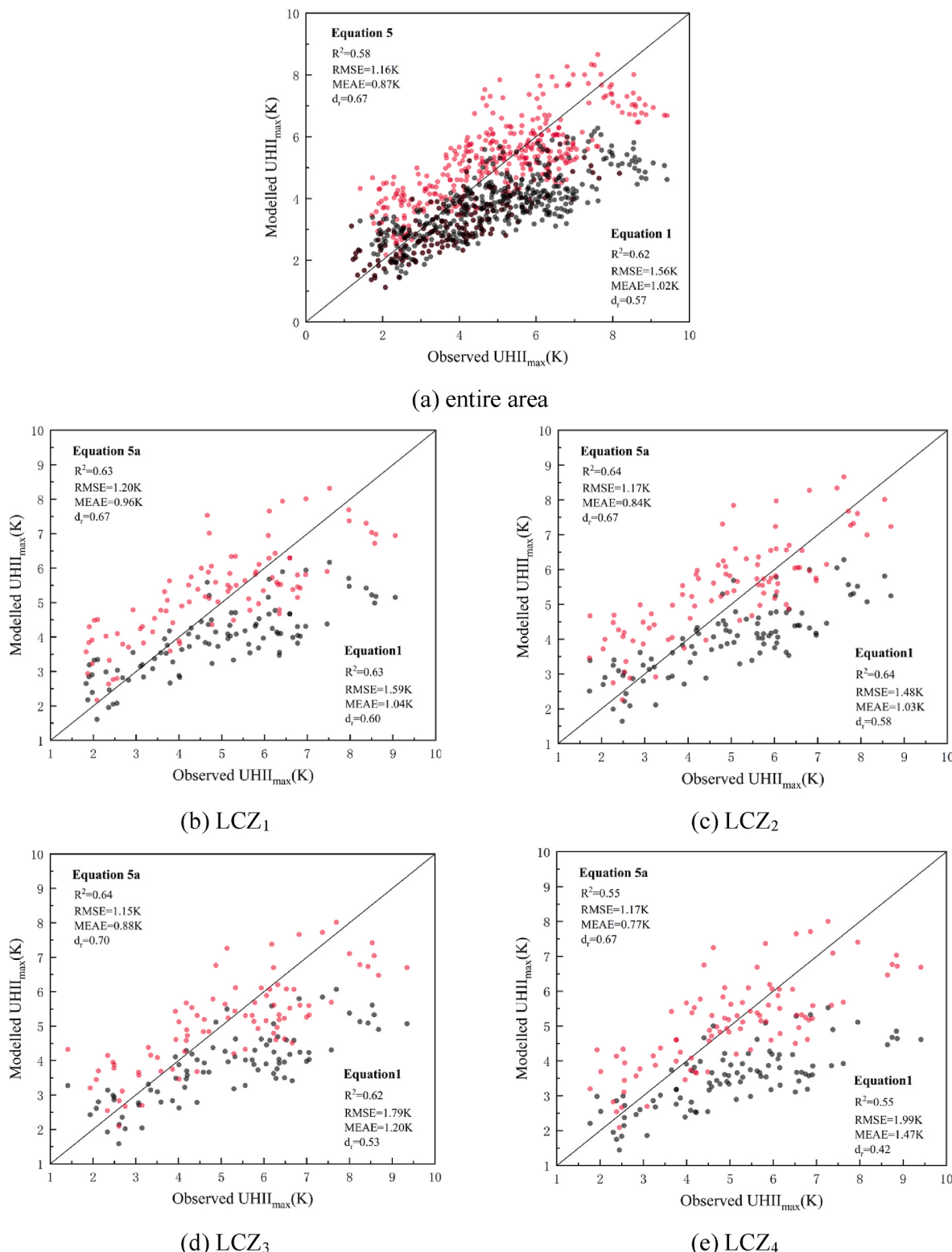


Fig. 9. Compared diagnostic effect of equations (1) and (5): (a) all LCZs; (b) LCZ₁; (c) LCZ₂; (d) LCZ₃; (e) LCZ₄, the black solid line is “y = x”.

(RMSE = 1.16 K, MEAE = 0.87 K, $d_r = 0.67$) was substantially improved, compared to that of equation (1) (RMSE = 1.56 K, MEAE = 1.02 K, $d_r = 0.57$).

In addition, the performance of the revised equation (equation (5a)) in LCZ_{1,2,3,4} were illustrated in Fig-s 9b–e. A similar trend was discerned for the LCZs, but the over-corrections were various in each LCZ. Quantitatively, according to the definition of overestimation and

underestimation for the model in section 3.2.2, the proportion of underestimation for equation (5a) is markedly decreased while the overestimation proportion is increased compared to equation (1). Then the moderate proportion with a significant enhancement of 6.5%, 15.2%, 26.2%, 27.2% respectively for LCZ_{1,2,3,4} (the details were listed in Table 5). Notably, a significant enhancement of the accuracy was discerned, especially in LCZ₄, where the RMSE decreased 0.82 K to 1.17K,

Table 5

Bias analysis comparison of revised and original equation for LCZ_{1,2,3,4}. The E₁ is abbreviation for equation (1) and E_{6a} is abbreviation for equation (5a).

	LCZ1		LCZ2		LCZ3		LCZ4
Bias interval(K)	E ₁	E _{5a}	E ₁	E _{5a}	E ₁	E _{5a}	E ₁
≥1.5	0	15	1	19	1	6	0
[1–1.5]	3	17	1	14	0	10	1
[0.5–1]	7	13	8	15	4	13	1
[0–0.5]	10	16	9	10	8	14	7
(-0.5–0)	18	8	14	18	13	10	11
(-1 – -0.5]	10	10	14	9	10	9	11
(-1.5 – -1]	16	6	13	7	11	12	15
(-2 – -1.5]	6	6	11	0	11	7	17
(-2.5 – -2]	8	1	12	0	8	2	10
(-3 – -2.5]	9	0	7	0	9	1	5
(-3.5 – -3]	3	0	2	0	7	0	7
≤-3.5	2	0	0	0	2	0	0
Total amounts	92	92	92	92	84	84	92
Underrated proportion	30.4%	7.6%	34.8%	0	44%	11.9%	50%
Overrated proportion	0	16.3%	1.1%	20.7%	1.2%	7.1%	0
Moderate proportion	69.6%	76.1%	64.1%	79.3%	54.8%	81%	50%
							77.2%

Table 6

Accuracy comparison for original and revised equation in all LCZs.

LCZ site	Type	R ²		RMSE		MEAE		d _r	
		original	revised	original	revised	original	revised	original	revised
All LCZs	–	0.62	0.58	1.56K	1.16K	1.02K	0.87K	0.57	0.67
LCZ ₁	Compact high-rise	0.63	0.63	1.59K	1.20K	1.04K	0.96K	0.60	0.67
LCZ ₂	Compact midrise	0.64	0.64	1.48K	1.17K	1.03K	0.84K	0.58	0.67
LCZ ₃	Compact low-rise	0.62	0.64	1.79K	1.15K	1.20K	0.88K	0.53	0.70
LCZ ₄	Open high-rise	0.55	0.55	1.99K	1.17K	1.47K	0.77K	0.42	0.67

the MEAE decreased 0.7 K to 0.77K and the d_r increased 0.25 to 0.67 (see the details in Table 6).

4. Discussion

4.1. Generalizing the results

This study applied the LCZ framework within a diagnostic equation proposed by a previous study, conducted in Europe. The diagnostic equation was validated and revised for a hot and humid Chinese city, Guangzhou. Overall, the diagnostic accuracy of the new equation was improved, not only for urban areas in general, but also for the independent LCZs. Indicatively, the revised equation can be used to calculate the daily *UHII_{max}* of different LCZs in Guangzhou.

As mentioned, UHI has global-scale effects and previous studies have addressed the correlation between UHI development and meteorology or morphology, thus paving the way for the revelation of quantitative laws behind. In general, there is a close association between *UHII* and *F_b* in Guangzhou according to the dimensional analysis. This indicates that meteorological parameters affect UHI in the same way as the discrepancy occurs in *A_i*. Ultimately, this fact allowed us to revise and optimize this equation according to the urban morphology.

The existing studies which applied this diagnostic equation are summarized in Table 7. As seen, this equation has been widely validated but not ultimately optimized, especially for hot and humid areas of south China.

4.2. Limitations and future studies

The introduction and methods of this study described the advantages of LCZs in details. In general, the equation proposed in this study can be used in the same LCZ type, but there is only one LCZ that corresponds to a LCZ category. Hence, it is necessary to validate it in other LCZs that have the same characteristics. During the field measurements period, some data were missing due to the instruments. In future studies, the

revised equation needs to be validated by using long-term data.

In urban areas, the anthropogenic heat flux (AHF) also contributes to the UHI, but the exact value is difficult to acquire. AHF varies significantly with latitude, season and population density [20]. Inherently, the optimal fitting coefficient (ideal *A_i*) depends on the *F_b*, and the “potential gap” in section 3.4 will change as the input of AHF varies, so inaccurate estimates of AHF will lead to an imprecise *A_i*. Furthermore, *F_b* is a meteorological indicator in suburban areas, it looks suitable for AHF to be added into *A_i* reflecting the properties in various urban areas, but seeking an appropriate way is necessary in future study. Therefore, the revised equation should not be applied to the LCZs with a large anthropogenic heat release. In addition, the thermal physical properties of building materials, such as surface albedo, were not considered in the revised equation. To make the equation be used quickly and conveniently, the stable and easily acquired indicators are preferred to use in our revised equation. As a parameter affecting the UHI, the surface albedo could be taken into consideration if various types of building in LCZ in Guangzhou or other cities in future study.

According to the fitting relationship between *UHII_{max}* and *F_b* and the underestimated proportion, the LCZs were classified into two categories. The field investigations pointed out a river at LCZ₅ (in front of the Guang yuan Secondary School) and LCZ₈ (Jun gong Road), as shown by satellite images in Fig. 1. In contrast, LCZ_{1,2,3,4} were characterized by large built-up area without cold sources. In this context, a previous study utilized remote sensing image data collected by ENVI software and combined this data with in-site observations collected by a weather station in Guangzhou to examine the influence of the Pearl River on the surrounding areas [52]. They showed that rivers can change the airflow of the surroundings, thereby exacerbating the wind speed near the river, compared to that in the densely built area of the city center. As a result, a lower *UHII* in the river surroundings was formed, compared to that of other areas. Notably, Fig-s 3, 4 and 5 illustrate this feature, but a longer dataset is likely required to ultimately confirm this pattern. In European research [31], the water fraction has been mentioned, where the authors have noted that water hampers the diurnal temperature range inside and

Table 7

Summary and review of the diagnostic equation research in various cities.

City	Climate characteristics	China building thermal zoning	dataset	Performance (original equation)	Review	Indicator added	Performance (revised equation)
Northwestern European cities [31]	mild maritime climate Köppen-Geiger system: Cfb	–	All seasons	$R^2 = 0.65$, RMSE = 0.91K, MEAE = 0.58K	Dimensional analysis and liner regression were combined to acquire the diagnostic equation, and the calculated $UHII_{max}$ is substantially closer to the observed one, exhibiting higher overall performance. However, the model would overestimate $UHII_{max}$ when the observed $UHII_{max}$ is low and underestimate conversely.	–	–
Nanjing, China [32]	Subtropical monsoon climate Köppen-Geiger system: Cfa	Hot summers and cold winters	Summer and winter	$R^2 = 0.46$, RMSE = 1.08K, MEAE = 0.76K	It represents the first attempt to assess the effectiveness of the diagnostic equation based on LCZ scheme outside of Europe. The equation slightly overestimates the UHII in all LCZs, but exhibits a good performance and it can be used to calculate $UHII_{max}$ in different LCZs. The author noted that it is necessary to seek for a reliable method of estimating the amount of anthropogenic heat release.	–	–
Xi'an, China [33]	Warm temperate semi-humid continental monsoon climate Köppen-Geiger system: Cwa	Cold areas	Summer	RMSE = 1.68K, MEAE = 1.14K	It does the first revision experiment in Chinese city. In validation of the original equation, it exhibits much more scatter and systematic difference: there are both overestimation and underestimation in urban areas. The class prediction with spatial categories based on the sum of "SVF" and " F_{veg} " was proposed, but use A_i to push back the urban morphology categories. Besides this, only summer conditions were considered.	BSF	RMSE = 1.35K, MEAE = 1.01K
Guangzhou, China	Oceanic subtropical monsoon climate Köppen-Geiger system: Cfa	Hot summers and warm winters	All seasons	$R^2 = 0.62$, RMSE = 1.56K, MEAE = 1.02K, $d_r = 0.57$	The validation and revision of the equation are both based on LCZ schemes. A larger deviation between modelled $UHII_{max}$ and observed one discerned. Moreover, an underestimation in all LCZs After revision, the accuracy of diagnostic equation model is improved.	ISF	$R^2 = 0.58$, RMSE = 1.16K, MEAE = 0.87K, $d_r = 0.67$

outside the city. However, this phenomenon was not considered in the original equation [31]. Additionally, study in Chengdu, China found that the cooling intensity logarithmically increased with the wetland size and the wetlands within the high-density building areas had a relatively high cooling efficiency [53]. In this context, quantitative classification is required for the scale of the water body in Guangzhou and other cities. Moreover, the LCZs with similar anomalies of LCZ₅ and LCZ₈, such as the cold source, should be thoroughly examined in future studies. In addition, given the seasonal characteristics of $UHII_{max}$, the accuracy of the original and revised equation was estimated depending on the season. The results and related seasonal comparison are shown in Fig. 10. As seen, in spring and summer, the red dots are mainly located above the line of "y = x" while the red dots are evenly distributed on both sides of the line for autumn and winter. The accuracy of the revised equation (5) was slightly lower than the original one in spring and summer (difference of RMSE and MEAE is 0.14K and 0.17K for spring, 0.11K and 0.18K for summer), but in autumn and winter it was markedly improved (difference of RMSE and MEAE is 0.74K and 0.62K for autumn, 0.5K and 0.24K for winter). Thus, the revised equation model requires further evaluation in future studies for maximizing its efficiency for seasonal applications.

5. Conclusions

For understanding the UHI effect, a simple and convenient method for quantifying the level of UHI development is required. To this end, a diagnostic equation of daily $UHII_{max}$ has been previously proposed and received considerable attention among scholars. Our study conducted

long-term temperature observation experiments based on LCZ framework in Guangzhou. Within the experiment, we quantified $UHII$ and $UHII_{max}$ for the selected 239 days during ~3 years and a revised equation for Guangzhou is proposed.

The analysis revealed an obvious variance for $UHII$ in spatiotemporal dimension. In particular, $UHII$ in autumn and winter was higher than that in spring and summer, while the $UHII$ of nighttime was higher than that of daytime. Moreover, $UHII$ and $UHII_{max}$ in LCZ₅ and LCZ₈ were markedly lower than LCZ_{1,2,3,4}. On this basis, the performance of equation was estimated using the dataset A of 147 days from July 2019 to April 2021. As a result, a significant correlation between $UHII_{max}$ and F_b was discerned on one hand. In contrast, the underestimation with a lower accuracy was identified (RMSE = 1.47 K, MEAE = 0.92 K, $d_r = 0.61$). The optimal fitting coefficient, called "ideal A_i " of LCZ_{1,2,3,4} was found outside the application range of original equation. Being combined with spatial characteristics of $UHII$ and $UHII_{max}$, the six LCZs were classified into two categories: (1) LCZ_{1,2,3,4} and (2) LCZ_{5,8}. Finally, a revised equation for LCZs was proposed, where dataset B of 92 days from May 2021 to April 2022 was utilized for validating the new equation. Notably, the accuracy of the revised equation was significantly improved (RMSE = 1.16, MEAE = 0.87, $d_r = 0.67$) compared to that of the original equation (RMSE = 1.56, MEAE = 1.02, $d_r = 0.57$). Moreover, it requires validation in other same LCZs for a universal application and the seasonal performance should be attach more attention. Overall, the study combined the diagnostic equation with LCZ scheme, then a simple and quick method for estimating the development level of UHI was proposed and could be used to calculate the daily $UHII_{max}$ of different LCZs in Guangzhou but more LCZs with the same

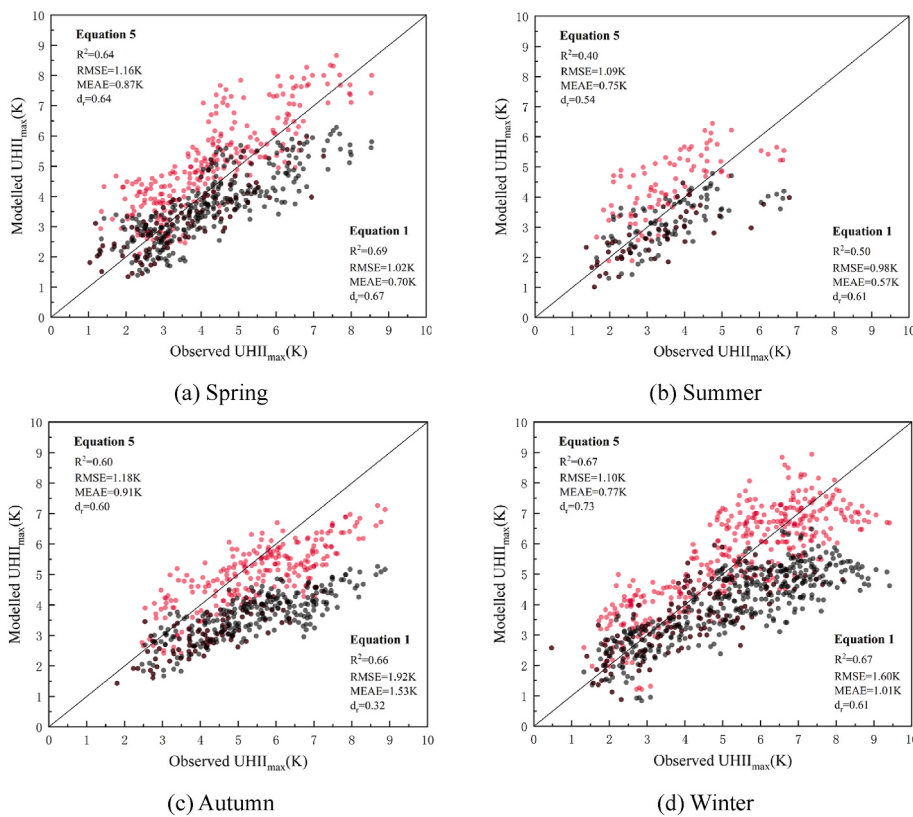


Fig. 10. The seasonally compared diagnostic effect of equation (1) and equation (5): (a) Spring; (b) Summer; (c) Autumn; (d) Winter.

characteristics should be examined. It will contribute to the monitoring of extreme thermal environment but a further study is needed to alleviate the remaining limitations.

CRediT authorship contribution statement

Guang Chen: Writing – review & editing, Writing – original draft, Visualization, Validation, Supervision, Software, Resources, Project administration, Methodology, Investigation, Funding acquisition, Formal analysis, Data curation, Conceptualization. **Hao He:** Writing – original draft, Visualization, Validation, Software, Methodology, Investigation, Formal analysis, Data curation, Conceptualization. **Yiqi Chen:** Visualization, Validation, Methodology, Investigation, Data curation. **Lihua Zhao:** Supervision, Project administration, Methodology, Conceptualization. **Yunnan Cai:** Supervision, Project administration, Funding acquisition. **Yuan Ma:** Supervision, Project administration.

Declaration of competing interest

The authors declare that they have no known competing financial interests or personal relationships that could have appeared to influence the work reported in this paper.

Data availability

Data will be made available on request.

Acknowledgements

This study was supported by the National Natural Science Foundation of China (No. 51708129, No.51978173). The authors acknowledge the anonymous reviewers for their helpful and constructive comments.

References

- [1] T. Oke, G. Mills, A. Christen, J. Voogt, *Urban Climates*, Cambridge University Press, London, 2017.
- [2] E.S. Darbani, D.M. Parapari, J. Boland, E. Sharifi, Impacts of urban form and urban heat island on the outdoor thermal comfort: a pilot study on Mashhad, *Int. J. Biometeorol.* 65 (7) (2021) 1101–1117, <https://doi.org/10.1007/s00484-021-02091-3>.
- [3] X. Wang, H.D. Li, S. Sodoudi, The effectiveness of cool and green roofs in mitigating urban heat island and improving human thermal comfort, *Build. Environ.* 217 (2022), <https://doi.org/10.1016/j.buildenv.2022.109082>.
- [4] S.P. Wang, Z.H. Wang, Y.C. Zhang, Y.F. Fan, Characteristics of urban heat island in China and its influences on building energy consumption, *Appl. Sci. Basel.* 12 (15) (2022), <https://doi.org/10.3390/app12157678>.
- [5] A. Aboelata, Vegetation in different street orientations of aspect ratio (H/W 1:1) to mitigate UHI and reduce buildings' energy in arid climate, *Build. Environ.* 172 (2020), <https://doi.org/10.1016/j.buildenv.2020.106712>.
- [6] P. Kabano, S. Lindley, A. Harris, Evidence of urban heat island impacts on the vegetation growing season length in a tropical city, *Landsc. Urban Plann.* 206 (2021), <https://doi.org/10.1016/j.landurbplan.2020.103989>.
- [7] Y.H. Zhang, P.Y. Yin, X.C. Li, Q.D. Niu, Y.X. Wang, W.T. Cao, J.X. Huang, H. Chen, X.C. Yao, L. Yu, B.G. Li, The divergent response of vegetation phenology to urbanization: a case study of Beijing city, China, *Sci. Total Environ.* 803 (2022), <https://doi.org/10.1016/j.scitotenv.2021.150079>.
- [8] Z.A. Rahaman, A. Kafy, M. Saha, A.A. Rahim, A.I. Almulhim, S.N. Rahaman, M. A. Fattah, M.T. Rahman, S. Kalaivani, A. Abdullah-Al-Faisal, A. Al Rakib, Assessing the impacts of vegetation cover loss on surface temperature, urban heat island and carbon emission in Penang city, Malaysia, *Build. Environ.* 222 (2022), <https://doi.org/10.1016/j.buildenv.2022.109335>.
- [9] Y.Q. Chen, B.Y. Shan, X.W. Yu, Study on the spatial heterogeneity of urban heat islands and influencing factors, *Build. Environ.* 208 (2022), <https://doi.org/10.1016/j.buildenv.2021.108604>.
- [10] X. Yang, Y. Chen, L.L.H. Peng, Q. Wang, Quantitative methods for identifying meteorological conditions conducive to the development of urban heat islands, *Build. Environ.* 178 (2020), <https://doi.org/10.1016/j.buildenv.2020.106953>.
- [11] Q.F. Huang, L. Li, Y.Q. Lu, Y.J. Yang, M.C. Li, The roles of meteorological parameters in Shanghai's nocturnal urban heat island from 1979 to 2013, *Theor. Appl. Climatol.* 141 (1–2) (2020) 285–297, <https://doi.org/10.1007/s00704-020-03214-3>.
- [12] X.S. Yang, Y. Chen, L.L.H. Peng, Q.Q. Wang, Quantitative methods for identifying meteorological conditions conducive to the development of urban heat islands, *Build. Environ.* 178 (2020), <https://doi.org/10.1016/j.buildenv.2020.106953>.

- [13] Z. Wu, Y. Ren, A bibliometric review of past trends and future prospects in urban heat island research from 1990 to 2017, *Environ. Rev.* 27 (2) (2019) 241–251, <https://doi.org/10.1139/er-2018-0029>.
- [14] S. Rahaman, S. Jahangir, M.S. Haque, R.S. Chen, P. Kumar, Spatio-temporal changes of green spaces and their impact on urban environment of Mumbai, India, *Environ. Dev. Sustain.* 23 (4) (2021) 6481–6501, <https://doi.org/10.1007/s10668-020-00882-z>.
- [15] P. Lin, D. Song, H. Qin, Impact of parking and greening design strategies on summertime outdoor thermal condition in old mid-rise residential estates, *Urban For. Urban Green.* 63 (2021), <https://doi.org/10.1016/j.ufug.2021.127200>.
- [16] N.I. Syafii, Promoting urban water bodies as a potential strategy to improve urban thermal environment, *Geographica Pannonica.* 25 (2) (2021) 113–120, <https://doi.org/10.5937/gp25-30431>.
- [17] F. Fan, Y. Wang, W.X. Yao, W.J. Gao, L.Y. Wang, Coupling mechanism of water and greenery on summer thermal environment of waterfront space in China's cold regions, *Build. Environ.* 214 (2022), <https://doi.org/10.1016/j.buildenv.2022.108912>.
- [18] K. Li, X.F. Li, K.J. Yao, Outdoor thermal environments of main types of urban areas during summer: a field study in wuhan, China, *Sustainability* 14 (2) (2022), <https://doi.org/10.3390/su14020952>.
- [19] G.G. Li, Z.H. Ren, C.H. Zhan, Sky View Factor-based correlation of landscape morphology and the thermal environment of street canyons: a case study of Harbin, *Chin Build. Environ.* 169 (2020), <https://doi.org/10.1016/j.buildenv.2019.106587>.
- [20] I.D. Stewart, T.R. Oke, Local climate zones for urban temperature studies, *Bull. Am. Meteorol. Soc.* 93 (12) (2012) 1879–1900, <https://doi.org/10.1175/BAMS-D-11-00019.1>.
- [21] G. Chen, M.J. He, N. Li, H. He, Y.N. Cai, S.L. Zheng, A method for selecting the typical days with full urban heat island development in hot and humid area, case study in Guangzhou, China, *Sustainability* 13 (1) (2021), <https://doi.org/10.3390/su13010320>.
- [22] S. Top, D. Milosevic, S. Caluwaerts, R. Hamdi, S. Savic, Intra-urban differences of outdoor thermal comfort in Ghent on seasonal level and during record-breaking 2019 heat wave, *Build. Environ.* 185 (2020), <https://doi.org/10.1016/j.buildenv.2020.107103>.
- [23] L. Ma, Z.Y. Yang, L. Zhou, H. Lu, G.F. Yin, Local climate zones mapping using object-based image analysis and validation of its effectiveness through urban surface temperature analysis in China, *Build. Environ.* 206 (2021), <https://doi.org/10.1016/j.buildenv.2021.108348>.
- [24] X.L. Chen, Y. Xu, J.X. Yang, Z.F. Wu, H. Zhu, Remote sensing of urban thermal environments within local climate zones: a case study of two high-density subtropical Chinese cities, *Urban Clim.* 31 (2020), <https://doi.org/10.1016/j.uclim.2019.100568>.
- [25] M. Lehnert, S. Savic, D. Milosevic, J. Dunjic, J. Geletic, Mapping local climate zones and their applications in European urban environments: a systematic literature review and future development trends, *ISPRS Int. J. Geo-Inf.* 10 (4) (2021), <https://doi.org/10.3390/ijgi10040260>.
- [26] C.R. de Almeida, L. Furst, A. Goncalves, A.C. Teodoro, Remote sensing image-based analysis of the urban heat island effect in braganca, Portugal, *Environments* 9 (8) (2022), <https://doi.org/10.3390/environments9080098>.
- [27] P. Manandhar, L. Bande, A. Tsopoulos, P.R. Marpu, P. Armstrong, A study of local climate zones in abu dhabi with urban weather stations and numerical simulations, *Sustainability* 12 (1) (2020), <https://doi.org/10.3390/su12010156>.
- [28] R.Q. Du, J.Y. Song, X.J. Huang, Q. Wang, C. Zhang, O. Brousse, P.W. Chen, High-resolution regional modeling of urban moisture island: mechanisms and implications on thermal comfort, *Build. Environ.* 207 (2022), <https://doi.org/10.1016/j.buildenv.2021.108542>.
- [29] Z. Liang, S.Y. Wu, Y.Y. Wang, F.L. Wei, J. Huang, J.S. Shen, S.C. Li, The relationship between urban form and heat island intensity along the urban development gradients, *Sci. Total Environ.* 708 (2020), <https://doi.org/10.1016/j.scitotenv.2019.135011>.
- [30] B. Zhou, D. Rybski, J.P. Kopp, The role of city size and urban form in the surface urban heat island, *Sci. Rep.* 7 (1) (2017) 4791, <https://doi.org/10.1038/s41598-017-04242-2>.
- [31] N.E. Theeuwes, G.-J. Steeneveld, R.J. Ronda, A.A.M. Holtslag, A diagnostic equation for the daily maximum urban heat island effect for cities in northwestern Europe, *Int. J. Climatol.* 37 (1) (2017) 443–454, <https://doi.org/10.1002/joc.4717>.
- [32] L.Y. Yao, X.S. Yang, C.L. Zhu, T. Jin, L.L.H. Peng, Y.H. Ye, Evaluation of a diagnostic equation for the daily maximum urban heat island effect, 10TH international symposium on heating, Ventilate. Air Condition. ISHVAC2017 (2017) 2863–2870.
- [33] X. Zhang, G.-J. Steeneveld, D. Zhou, C. Duan, A.A.M. Holtslag, A diagnostic equation for the maximum urban heat island effect of a typical Chinese city: a case study for Xi'an, *Build. Environ.* 158 (2019) 39–50, <https://doi.org/10.1016/j.buildenv.2019.05.004>.
- [34] M. Kottek, J. Grieser, C. Beck, B. Rudolf, F. Rubel, World Map of the Köppen-Geiger climate classification updated, *Meteorol. Z.* 15 (3) (2006) 259–263, <https://doi.org/10.1127/0941-2948/2006/0130>.
- [35] C.M. Bureau, *China Standard Weather Data for Analyzing Building Thermal Conditions*, China Building Industry Publishing House, Beijing, 2005.
- [36] S.J. Jiang, X. Lee, J.K. Wang, K.C. Wang, Amplified urban heat islands during heat wave periods, *J. Geophys. Res. Atmos.* 124 (14) (2019) 7797–7812, <https://doi.org/10.1029/2018JD030230>.
- [37] Y. Sun, X.C. Zhang, Y. Zhao, Q.C. Xin, Monitoring annual urbanization activities in Guangzhou using Landsat images (1987–2015), *Int. J. Rem. Sens.* 38 (5) (2017) 1258–1276, <https://doi.org/10.1080/01431612.2016.1268283>.
- [38] G.M.B.O. Statistics, *Bulletin of the Seventh National Population Census of Guangzhou, 2021, Guangzhou*.
- [39] T. Peng, C. Sun, S. Feng, Y. Zhang, F. Fan, Temporal and spatial variation of anthropogenic heat in the central urban area: a case study of Guangzhou, China, *ISPRS Int. J. Geo-Inf.* 10 (3) (2021), <https://doi.org/10.3390/ijgi10030160>.
- [40] X.S. Yang, L.Y. Yao, T. Jin, L.L.H. Peng, Z.D. Jiang, Z.Y. Hu, Y.H. Ye, Assessing the thermal behavior of different local climate zones in the Nanjing metropolis, China, *Build. Environ.* 137 (2018) 171–184, <https://doi.org/10.1016/j.buildenv.2018.04.009>.
- [41] M. Bruse, H. Fleer, Simulating surface-plant-air interactions inside urban environments with a three dimensional numerical model, *Environ. Model. Software* 13 (3–4) (1998) 373–384, [https://doi.org/10.1016/S1364-8152\(98\)00042-5](https://doi.org/10.1016/S1364-8152(98)00042-5).
- [42] A.G. Davenport, C. Grimmond, T. Oke, J. Wieringa, Estimating the roughness of cities and sheltered country, in: *15th Conference on Probability and Statistics in the Atmospheric Sciences/12th Conference on Applied Climatology*, American Meteorological Society, Asheville, NC, 2000, pp. 96–99.
- [43] T. He, S. Liang, D. Wang, Y. Cao, F. Gao, Y. Yu, M. Feng, Evaluating land surface albedo estimation from Landsat MSS, TM, ETM +, and OLI data based on the unified direct estimation approach, *Rem. Sens. Environ.* 204 (2018) 181–196, <https://doi.org/10.1016/j.rse.2017.10.031>.
- [44] B. Souhail, B. Giampaolo, D. Emanuel, B. Anton, C. Albergel, *Analysis of Surface Albedo and Leaf Area Index from Satellite Observations and Their Impact on Numerical Weather Prediction*, ECMWF, 2014.
- [45] C.J. Willmott, S.M. Robeson, K. Matsuurra, A refined index of model performance, *Int. J. Climatol.* 32 (13) (2012) 2088–2094, <https://doi.org/10.1002/joc.2419>.
- [46] J.D. Evans, *Straightforward Statistics for the Behavioral Sciences*, Thomson Brooks/Cole Publishing Co., 1996.
- [47] J.J. Ge, Y.P. Wang, H. Akbari, D. Zhou, The effects of sky view factor on ground surface temperature in cold regions - a case from Xi'an, China, *Build. Environ.* 210 (2022), <https://doi.org/10.1016/j.buildenv.2021.108707>.
- [48] Y.H. Chen, J.T. Wu, K. Yu, D.D. Wang, Evaluating the impact of the building density and height on the block surface temperature, *Build. Environ.* 168 (2020), <https://doi.org/10.1016/j.buildenv.2019.106493>.
- [49] D. Dutta, A. Rahman, S.K. Paul, A. Kundu, Impervious surface growth and its interrelationship with vegetation cover and land surface temperature in peri-urban areas of Delhi, *Urban Clim.* 37 (2021), <https://doi.org/10.1016/j.uclim.2021.100799>.
- [50] Z.Q. Yu, S.S. Chen, N.H. Wong, Temporal variation in the impact of urban morphology on outdoor air temperature in the tropics: a campus case study, *Build. Environ.* 181 (2020), <https://doi.org/10.1016/j.buildenv.2020.107132>.
- [51] J.H. Xu, Y. Zhao, C.G. Sun, H.B. Liang, J. Yang, K.W. Zhong, Y. Li, X.L. Liu, Exploring the variation trend of urban expansion, land surface temperature, and ecological quality and their interrelationships in Guangzhou, China, from 1987 to 2019, *Rem. Sens.* 13 (5) (2021), <https://doi.org/10.3390/rs13051019>.
- [52] X.Y. Du, Q. Li, The effect of Pearl River on summer urban thermal environment of Guangzhou, in: *10TH INTERNATIONAL SYMPOSIUM ON HEATING, VENTILATION AND AIR CONDITIONING, ISHVAC2017, 2017*, pp. 1785–1791.
- [53] S.J. Wu, H. Yang, P. Luo, C.A. Luo, H.L. Li, M. Liu, Y. Ruan, S.J. Zhang, P. Xiang, H. H. Jia, Y. Cheng, The effects of the cooling efficiency of urban wetlands in an inland megacity: a case study of Chengdu, Southwest China, *Build. Environ.* 204 (2021), <https://doi.org/10.1016/j.buildenv.2021.108128>.